

We are IntechOpen, the world's leading publisher of Open Access books Built by scientists, for scientists

6,900

Open access books available

186,000

International authors and editors

200M

Downloads

Our authors are among the

154

Countries delivered to

TOP 1%

most cited scientists

12.2%

Contributors from top 500 universities



WEB OF SCIENCE™

Selection of our books indexed in the Book Citation Index
in Web of Science™ Core Collection (BKCI)

Interested in publishing with us?
Contact book.department@intechopen.com

Numbers displayed above are based on latest data collected.
For more information visit www.intechopen.com



Laser Micromachining and Micro-Patterning with a Nanosecond UV Laser

Xianghua Wang¹, Giuseppe Yickhong Mak² and Hoi Wai Choi²

¹Key Lab of Special Display Technology, Ministry of Education,
National Engineering Lab of Special Display Technology,
National Key Lab of Advanced Display Technology,
Academy of Photoelectric Technology,
Hefei University of Technology, Hefei,

²Department of Electrical and Electronic Engineering,
The University of Hong Kong,

¹China

²Hong Kong

1. Introduction

Laser micromachining specifically refers to drilling and cutting with intensive laser beam usually in the form of pulse trains with energy far exceeding the ablation threshold of the target material. The ablation threshold, however, is dependent on material properties as well as the interacting laser characteristics such as laser wavelength and pulse width. Therefore, laser processes are flexible and can be highly selective. Laser wavelengths have been available in a wide spectrum range from the far infrared to the ultraviolet using a variety of medium material and frequency mixing techniques. Since late 1990s, ultra short laser beams (Gattass and Mazur 2008; Liu, et al. 1997; Molian, et al. 2009; Schaffer, et al. 2001; Stuart, et al. 1996; Varel, et al. 1997) from picosecond to femtosecond are intensively studied as to their interaction mechanism with transparent materials and applications in material processing. Although ultra short pulses within tens of picoseconds can be achieved by advanced techniques like Q-switching and mode-locking, the pulse energy is reduced by several orders of magnitude and the laser system is relatively bulky. Nanosecond lasers with intermediate pulse width are still predominant in industry due to their excellent flexibility and cost effectiveness. This chapter presents the work in laboratory on laser micromachining and micro-patterning of GaN/sapphire LED wafer with nanosecond UV laser for the purpose of chip-shaping and device isolation respectively.

2. Laser micromachining

2.1 Laser-matter interaction

Interaction of material with laser pulses generally involves the following fundamental processes that take place on different time scales after a pulse incidence (Zweig 1991). Firstly, light absorption takes place at a femtosecond time scale accompanied by ejection of

excited electrons. Secondly, the excited electrons transfer their energy to the lattice in several tens of picoseconds through electron-phonon collision and induce melted zone in the bulk material. Following this, melted material evaporates on a nanosecond time scale and expands into the air in the form of atomic-sized particles in the ablation plume. Melt expulsion may also occur, termed hydrodynamic ablation, due to the recoil pressure of plume and result in large particles or clusters following the plume.

The specific ablation mechanism in laser micromachining and the resulting morphology of the ablated region such as aspect ratio and sidewall roughness varies with material property, laser wavelength, power intensity as well as pulse duration. The process of multiphoton excitation of electrons and collisional ionization is reported to play vital roles in semiconductor and dielectric laser ablation with a sharp threshold of power intensity observed. This mechanism become dominant when ultra-short laser pulses are employed for ablation, whereby a much increased portion of laser energy is transferred to electrons compared to the portion further transferred to the lattice (Stuart, et al. 1996). Under high intensity picosecond-pulsed laser fluence, the laser irradiated portion of n-type SiC material can be directly transformed into plasma on a few picoseconds time scale through Coulomb explosion resulting in clean surfaces of the cleaves that outperform the results obtained with thermal ablation (Molian, et al. 2009).

2.2 Optical setup of laser micromachining

The laser micromachining system consists of a UV laser source, beam focusing optics and an x-y motorized translation stage. The laser source used in this experiment is a third harmonic neodymium-doped yttrium lithium fluoride (ND:YLF) diode-pumped solid-state (DPSS) laser manufactured by Spectra Physics. Being an actively Q-switched UV laser at 349 nm, the pulse repetition rate ranges from single pulse to 5 kHz. At the reference diode current of 3.2A, the pulse energy is 120 μJ with a pulse width of around 4 nanoseconds at 1 kHz repetition rate; however, this corresponds to very high intensity up to the order 10^{10} W/cm² when focused to a 10- μm -diameter spot.

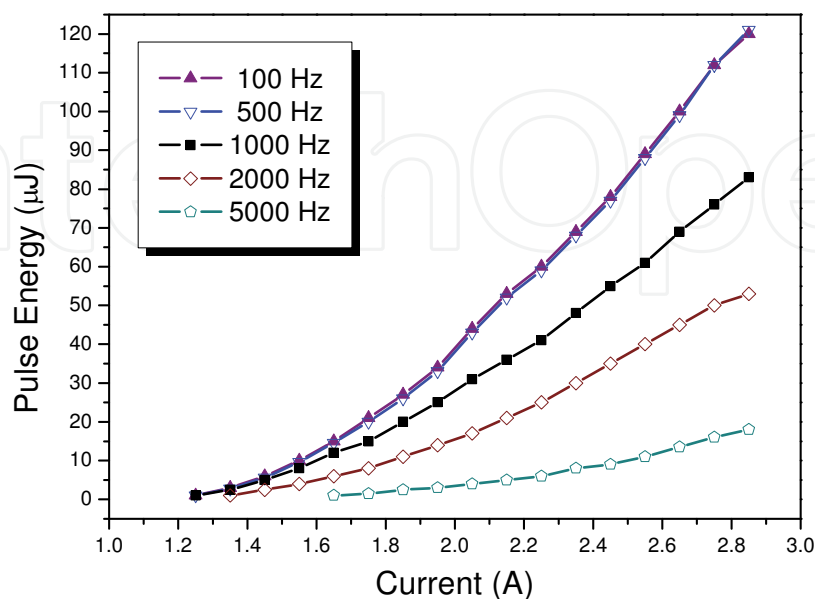


Fig. 1. Pulse energy versus diode current at different pulse repetition rates

The beam intensity distribution is a Gaussian profile. There is a compromise between the pulse energy and the pulse repetition rate. According to the plots of pulse energy versus diode current recorded at a series of repetition frequencies, the pulse energy at lower repetition frequency goes higher until the repetition frequency is lower than 500 Hz as indicated in Figure 1.

As a smaller focus spot, which is diffraction limited, is desired for micro-scale machining, laser of shorter wavelength is preferred. The TEM₀₀ beam in our laser source also allows for tight focusing, offering high spatial resolution. After beam expansion and collimation through a beam expander, the laser beam is reflected 90° by a dielectric laser line mirror and focused onto the horizontal machining plane to a very tiny spot several micrometers in diameter with a focusing triplet. The UV objective lens well suits the Gaussian beam profile of the laser. All optics are made of UV fused silica and anti-reflection coated. The size of the beam at the focal point is not only limited by the capability of the UV objective lens but is also sensitive to the coaxiality of the optics. Schematic diagram of the laser micromachining setup is drawn in Figure 2. A pair of aluminium mirrors is used to adjust the direction of the collimated laser beam to be coaxial with the UV objective lens.

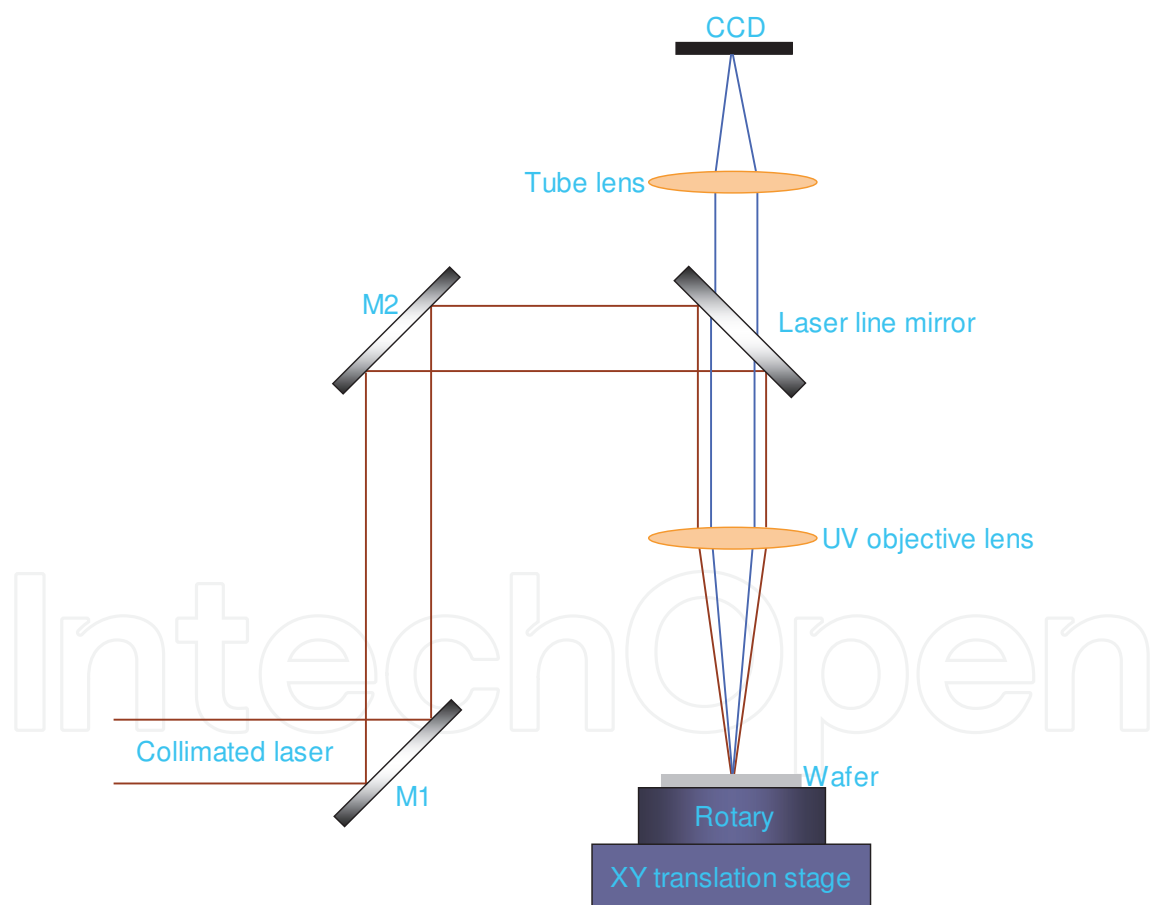


Fig. 2. Schematic of laser micromachining setup

The additional feature of the set-up for tilted cutting, as illustrated in Figure 3, is the insertion of a UV mirror at an oblique angle within the optical path between the focusing optics and the machining plane, which serves to deflect the convergent beam to strike the sample at an oblique angle with respect to the horizontal working plane. With this modified

set-up, it is relatively easy to optimize and monitor the beam through the tube lens imaged with a CCD camera. Once the optical setup is optimized before insertion of the tilting mirror, the mirror can be inserted without affecting the coaxiality of the laser beam.

The beam can be effectively applied for micro-sectioning with non-vertical sidewall profiles. The angle of incidence of the deflected laser beam on the wafer is 2θ , where θ as indicated in Figure 3 is the angle between the plane of the mirror and the normal. This angle is readily and precisely controlled by mounting the mirror onto a rotation stage; thus, the incident angle can be varied over a wide range. In this experiment, we have used a UV objective with a focal length of 75 mm, based on two considerations. Firstly, the focal length should be long enough to accommodate the mirror in the optical path. Secondly, an ideal tool for the fabrication of microstructures should have a very long penetration depth and negligible lateral dispersion. Nevertheless, an objective lens with a longer focal length also produces a larger focused beam spot. The diameter of the focused beam spot, d , is determined by the following equation:

$$d = \frac{4\lambda M^2 f}{\pi D} \quad (1)$$

where M^2 is the beam quality factor, λ the wavelength of the laser beam, f the focal length and D the diameter of the incident beam.

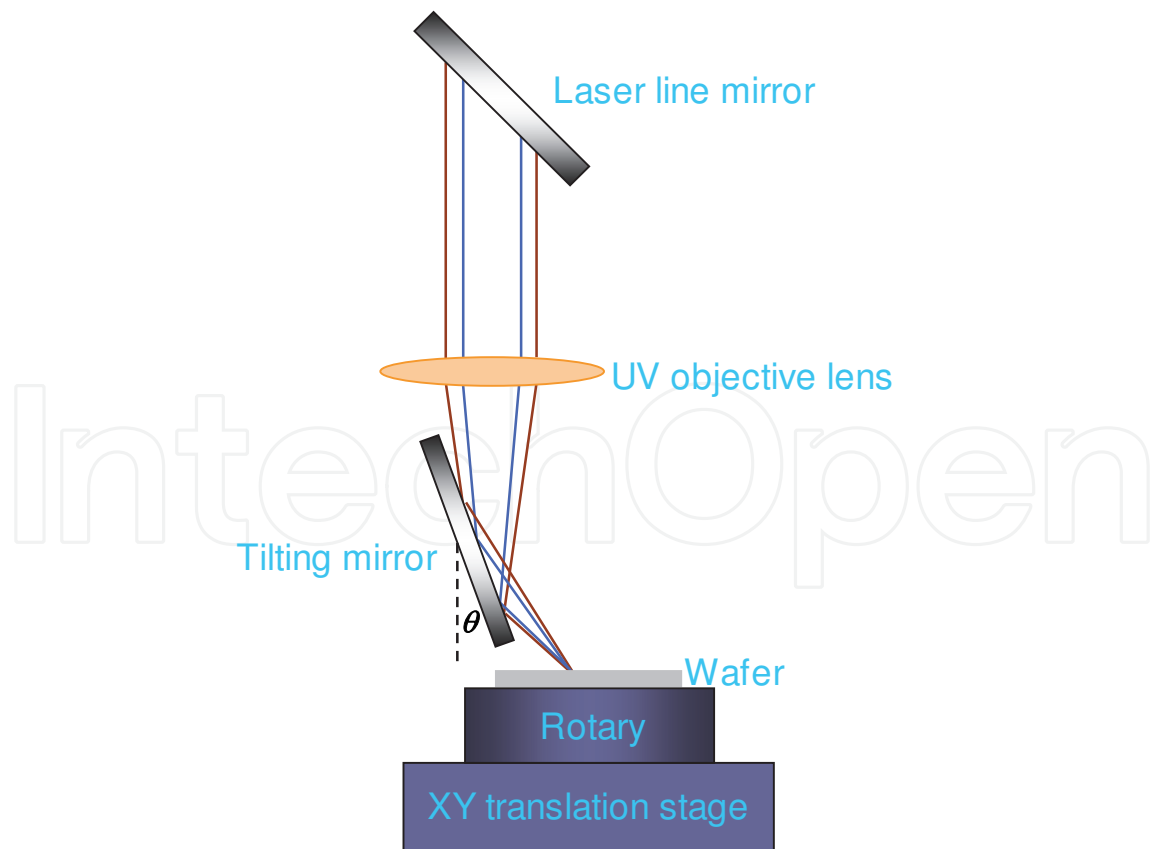


Fig. 3. Schematic of the setup for tilted-cutting with a UV mirror inserted within the optical path

2.3 Laser cutting of sapphire wafer

As our scheme of micromachining is targeted at die separation of GaN-based LEDs, sapphire wafers are used for testing the results, as it is the typical substrate for the metalorganic chemical vapour deposition (MOCVD) growth of GaN. The quality of the cleave can be quantified by the width, depth, linearity and sidewall roughness of the trench formed by the laser beam. Each of these parameters will be investigated. Since the focal length of the focusing lens ($f = 75 \text{ mm}$) is much longer than the thickness of the sapphire wafer ($t = 420 \text{ }\mu\text{m}$), the depth of the trench mainly depends on the number of micromachining cycles. The number of cycles is controlled by configuring the translation stage to repeat its linear path over a number of times. Since the position repeatability of the stage is better than $5 \text{ }\mu\text{m}$, increasing the number of cycles should not contribute significantly to the width of the feature. Figure 4 shows the cross-sectional optical image of a $420 \text{ }\mu\text{m}$ thick sapphire wafer that has been micro-machined with an incident beam inclined at 45° , with scan cycles ranging from 1 to 10. These incisions were carried out by setting the laser pulse energy to $54 \text{ }\mu\text{J}$ at a repetition rate of 2 kHz . The relationship between the inclined cutting depth and the number of passes of the beam are plotted in Figure 5. After the first pass of the beam, a narrow trench with a width of $\sim 20 \text{ }\mu\text{m}$ and a depth of $\sim 220 \text{ }\mu\text{m}$ was formed. Successive scans of the beam along the trench results in further deepening and widening, but the extent was increasing less. The depth of the trench depends on the effective penetration of the beam. From the second scan onwards, the beam has to pass through the narrow gap before reaching the bottom of the trench for further machining. The energy available at this point is attenuated, partly due to lateral machining of the channel (causing undesirable widening), absorption and diffraction effects. Therefore, the depth of the trench tends to saturate after multiple scans.

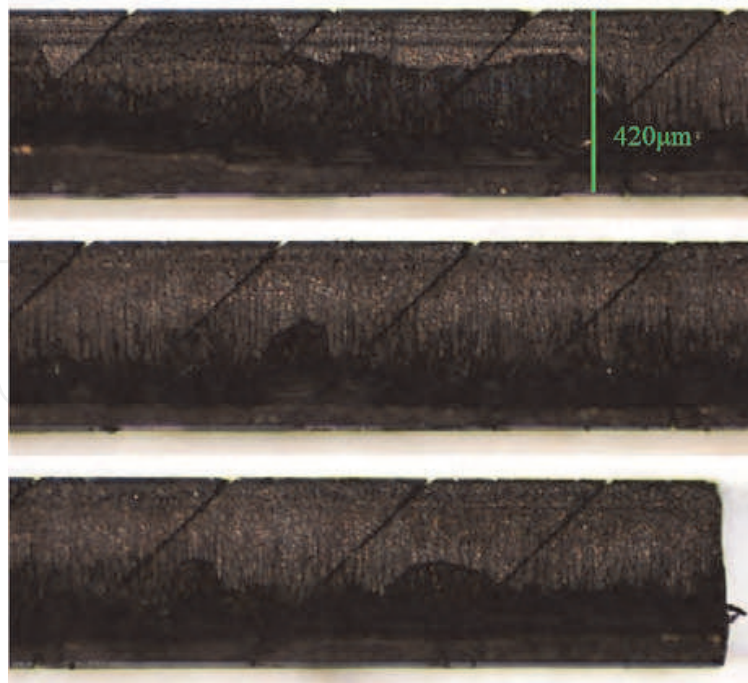


Fig. 4. Cross-sectional optical microphotograph of laser micro-machined micro trenches at an inclination angle of $\sim 45^\circ$ at a range of scan cycles of between 1 and 10 (left to right then down). (with permission for reproduction from American Institute of Physics)

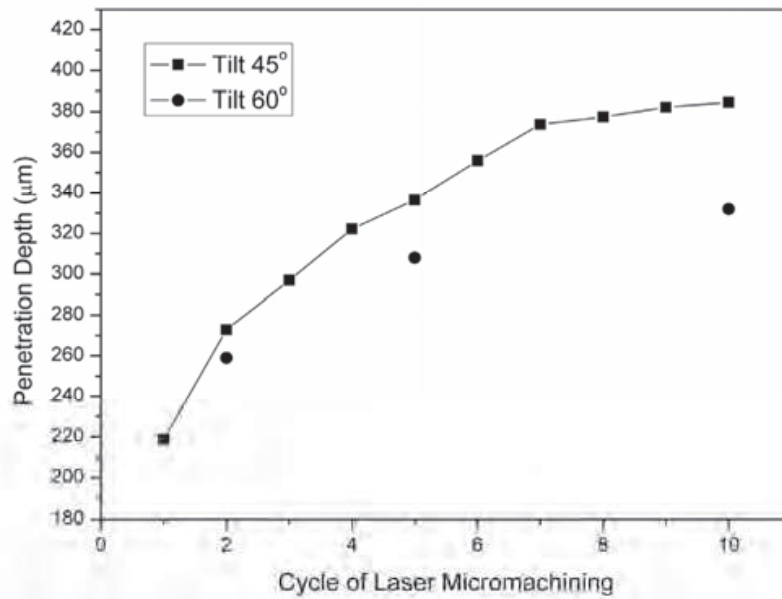


Fig. 5. Depth of tilting micro-trenches as a function of scan cycles. (with permission for reproduction from American Institute of Physics Publishing)

After the chemical treatment, the surface morphologies of the micromachined samples are examined with atomic force microscopy (AFM). 3D images of the AFM scans are shown in Figure 6. The surface topography of the sapphire surface after 2 machining cycles exhibits a uniform roughness with an RMS value of ~ 150 nm. With more cycles, increasing densities and dimensions of granules are observed on the AFM image and the RMS roughness increased to ~ 218 nm after 5 cycles. The formation of the larger grains on the surface is a result of uneven aggregation and re-solidification of the melted material. The evacuation rate of the ablated species declines as the beam reaches deeper into the trench, and statistically the density of aggregation is more pronounced at these deeper sites.

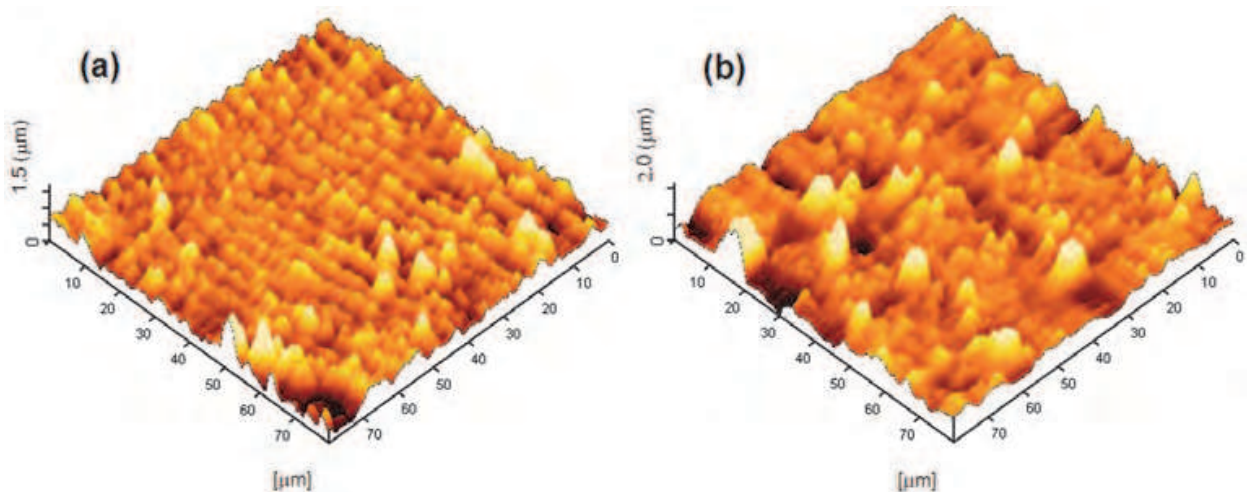


Fig. 6. AFM morphology images of the inclined sapphire surfaces after laser micromachining for (a) 2 cycles and (b) 5 cycles, the corresponding RMS roughness are 150 nm and 218 nm respectively. (with permission for reproduction from American Institute of Physics)

2.4 Front-side Laser micromachining of GaN/sapphire LED wafer

In our laser micromachining setup, using 349 nm wavelength, a front-side machining scheme is employed to avoid damage to the active-layer as well as to achieve higher precision with beam alignment. A tilted incision with 60° ($\theta=30^\circ$) tilting angle on the front side of the GaN/sapphire wafer is ablated after 5 successive scan cycles. The surface of the sidewall is exposed after laser micromachining for FE-SEM examination as shown in Figure 7. With the laser beam tightly focused, the kerf exposed at GaN layer shows a clear brim and the thickness of GaN estimated from the image is $4.5\ \mu\text{m}$. It is interesting to see a sharp interface between the sapphire substrate and the GaN layer and no heat affected zone (HAZ) is observed in the GaN layer after front-side machining. This finding may be attributed to the relatively low ablation threshold of GaN as it absorbs the 349 nm laser power. According to Figure 7, the sapphire substrate melts on the surface, while no melt is observed for the GaN layer. It is estimated that the surface temperature lies between the melting point of sapphire and GaN, which is in the range from $2040\ ^\circ\text{C}$ to $2500\ ^\circ\text{C}$.

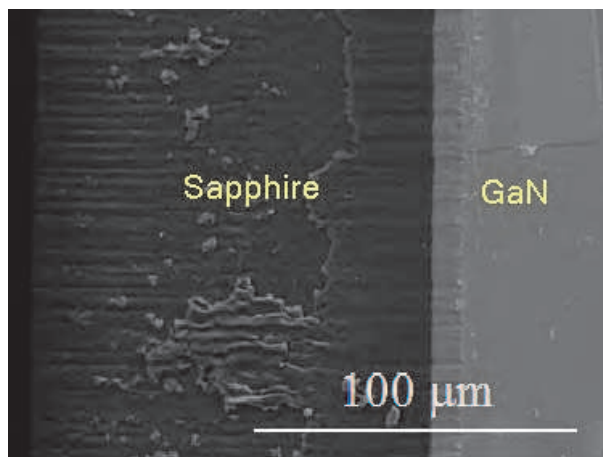


Fig. 7. FE-SEM image of a GaN/sapphire wafer after laser micromachining, the interface of GaN and sapphire and the brim of the $4.5\ \mu\text{m}$ thick GaN layer is clear.

For comparison, surface morphology of backside micromachined LED wafer is illustrated in Figure 8 showing the feature of rugged sidewalls. The two images corresponds to a single scan of the laser beam at $50\ \mu\text{m}/\text{sec}$ motion speed, with $30\ \mu\text{J}$ and $50\ \mu\text{J}$ pulse energy respectively, repeated at 1 kHz. This feature can be observed at varied pulse energies and scan cycles. With a high ablation threshold and optical transparency at the wavelength of 349 nm, sapphire is ablated with inferior surface quality. A large quantity of clusters is trapped within the groove which blocks light extraction from the sidewalls and also prevents heat dissipation via the sidewall surfaces. Improved quality of sapphire micromachining is possible by using a shorter wavelength or ultrashort pulse duration of the laser to suppress thermal effect during sapphire ablation. Laser ablation of the sapphire substrate with an absorptive wavelength to sapphire also avoids damaging on the epitaxial nitride layers.

Separation of some specially shaped LED such as a circular device after laser micromachining may be difficult if the wafer is cut insufficient in depth. The chips to be separated after machining are subject to uncontrollable fracture and crack whilst applying stress to the incision. In order to shape circular LEDs, the machining has to penetrate through the wafer to ensure separation in good shape. Although the penetration depth

depends on laser power, it is important to adjust the focus position in the z direction in order to optimize the process condition.

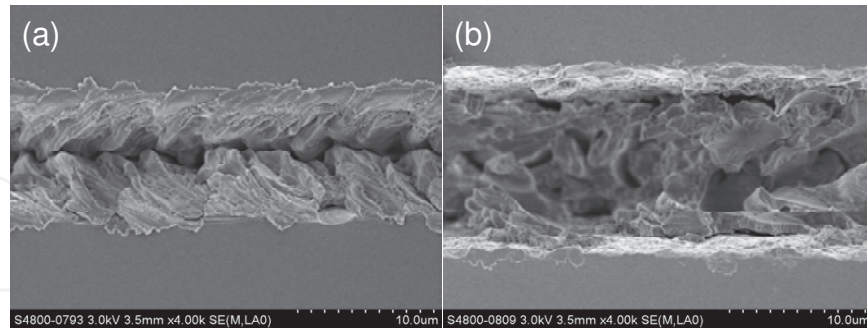


Fig. 8. (a) SEM image of laser scribed lanes on the back-side sapphire substrate with 30 μJ pulses; (b) with 50 μJ pulses

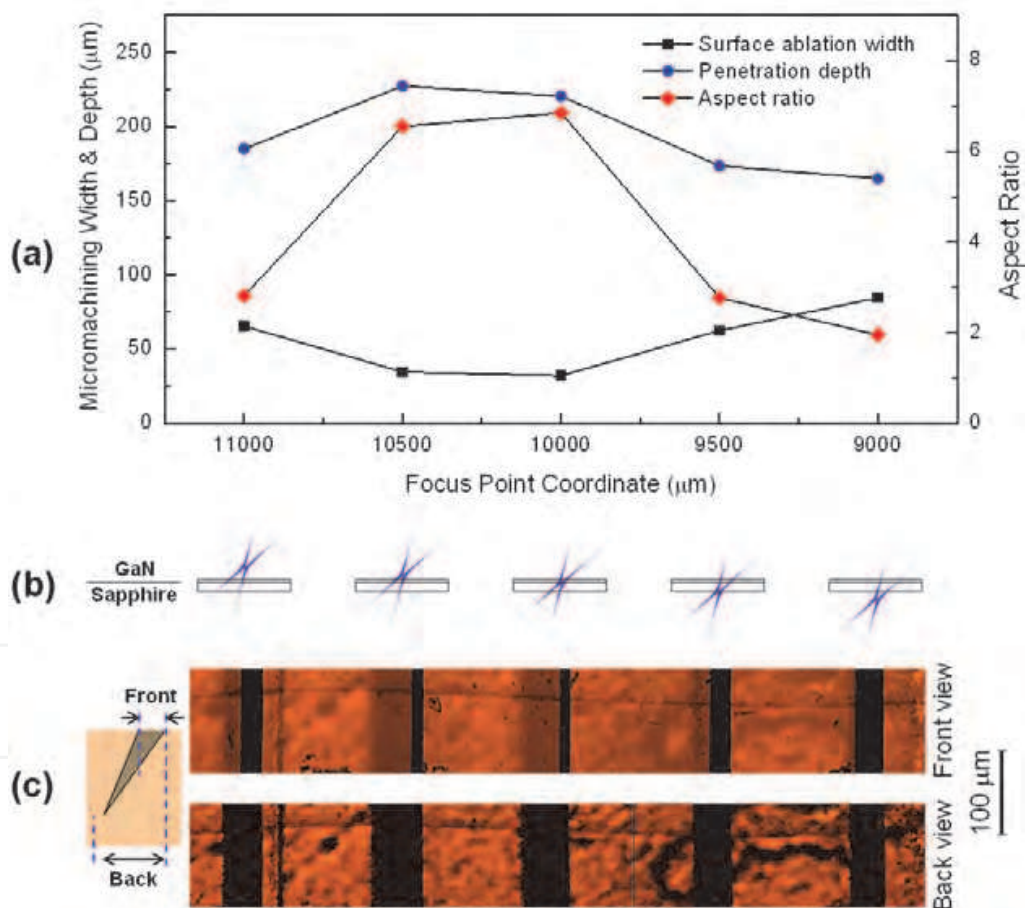


Fig. 9. (a) Trends of surface ablation width, penetration depth and the aspect ratio with changing focusing levels during micromachining; (b) Relative position of the focus point with reference to the wafer; (c) The width of surface damage determined from front view of wafer, and penetration depth estimated from the back view (mirrored) after laser micromachining at 40° tilting angle. (with permission for reproduction from John Wiley and Sons)

Figure 9 shows the surface ablation widths and penetration depths of the incisions machined at 40° tilting angle from the vertical. The pulse energy is about $90 \mu\text{J}$ with a pulsed repetition rate of 1 kHz. The beam is scanned over a round trip cycle at a constant scan speed of $50 \mu\text{m}/\text{sec}$. Figure 9 (a) plots the measured dimensions with relation to a sequence of focal positions. The relative positions of the focal spot with respect to the wafer are depicted in Figure 9 (b). The surface ablation widths and penetration depths are estimated from the front and the back view optical microscopy images as shown in Figure 9 (c). The position where laser focal point coincides with the surface of GaN is recorded at the z coordinate of $9900 \mu\text{m}$. The optimized region for micromachining spans over the range of $[10000, 10500]$ as the surface ablation width is at minimum while the penetration depth and aspect ratio are at maximum values. It is also found that when the wafer deviate from the focus position there is a chance of beam deformation and induce additional scribing run parallel to the desired groove. This is observed at the coordinate of 11000 as shown on the leftmost in Figure 9 (c).

2.5 Chip shaping of light-emitting diodes to improve light extraction

Light extraction from GaN-based light-emitting diodes is seriously suppressed by total internal reflections within the semiconductor layers. With a high refractive index around 2.4, light extraction from the top surface is limited within a 23° emission cone as depicted in Figure 10 (c). One effective method to enhance light extraction is employing tilting sidewalls such as those in a truncated pyramid (TP) LED, where the conventionally confined light rays are extracted from the top surface via sidewall reflections that redirect the light ray into the top surface emission cone. Accordingly, top surface emission of a laser fabricated TP LED shown in Figure 10 (b) is particularly stronger compared to the conventional rectangular chip in (a). The overall light extraction can be enhanced by 85%. The improvement is attributed to the additional indirect light extraction from top surface via sidewall reflections.

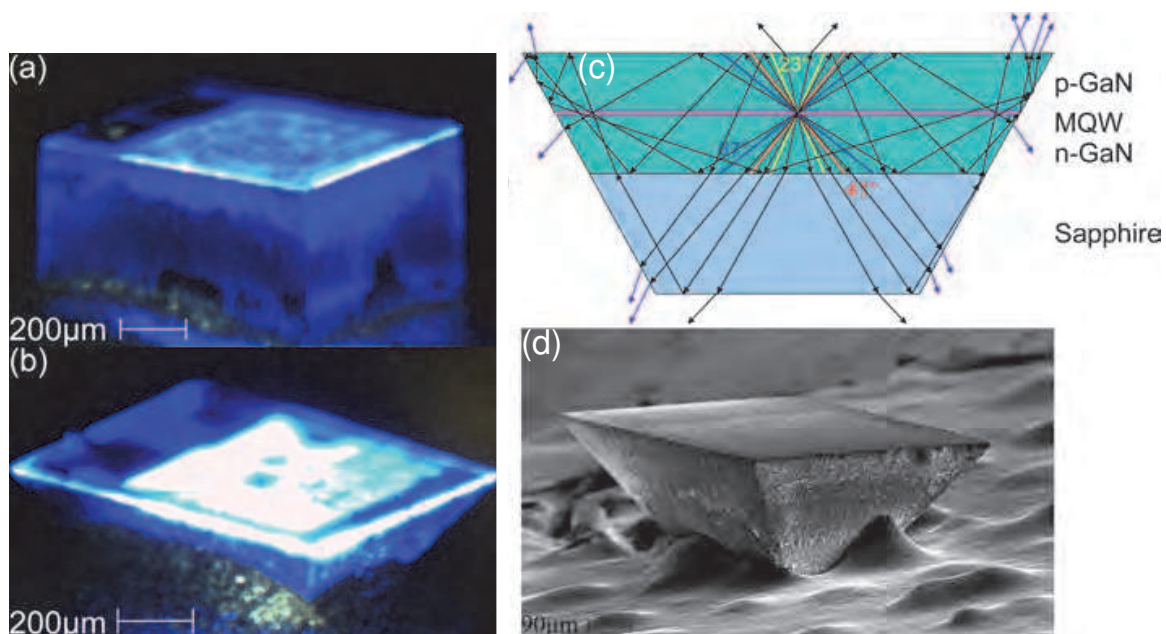


Fig. 10. Optical micrographs of (a) conventional cuboid LED and that of (b) truncated pyramid LED with tilting sidewall, (c) schematic diagram of enhanced top surface light extraction via sidewall reflections. (d) SEM image of the truncated pyramid LED chip shaped by laser micromachining. (adapted from (Fu, et al. 2009) with permission for reproduction from IEEE)

Additional indirect light extraction also exists in a triangular LED, making it unique among polygonal LEDs. However, the mechanism is slightly different with that of a TP LED. In a triangular LED chip, enhanced light extraction is due to indirect light extraction from the sidewall via reflections on neighbouring sidewalls, while in the case of a rectangular chip or other polygons, the indirect extraction is trivial. Actual chip geometry from triangle to heptagon are fabricated with the laser micromachining system and shown in Figure 11.

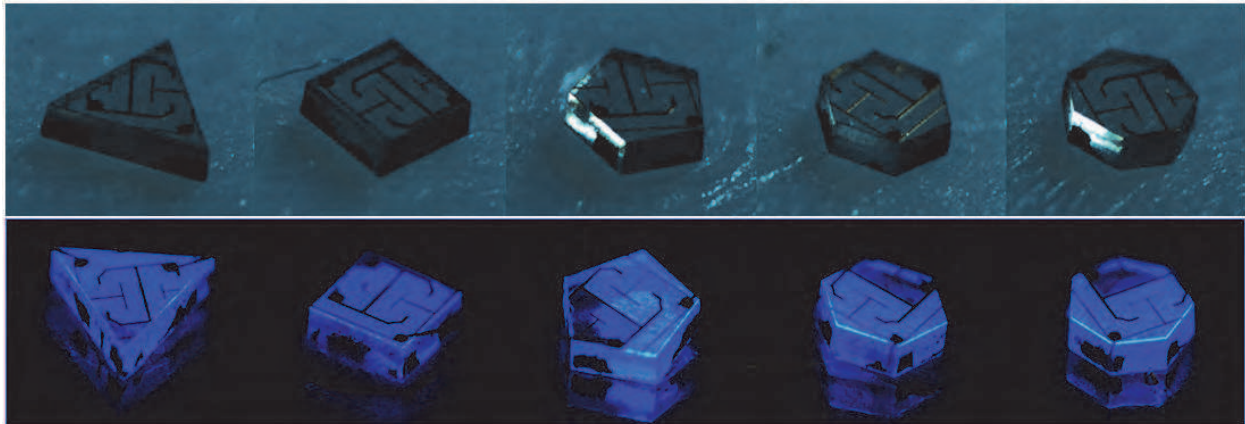


Fig. 11. Optical Micrograph Polygonal LEDs as fabricated by laser beam (upper row) and biased at 2.5 V (lower row). (with permission for reproduction from American Institute of Physics)

3. Device isolation on GaN-on-sapphire wafer via laser micro-patterning

GaN is the major material for the fabrication of state-of-the-art blue light-emitting diodes. It is conventionally grown on sapphire substrates by metalorganic chemical vapour deposition (MOCVD), since sapphire is stable and can withstand the high temperature during the growth process. Although there are many issues involved with sapphire, such as lattice mismatch with GaN and poor heat conductivity, sapphire is still prevalent in the fabrication of low-power blue and white LEDs. In addition, being an electrical insulator, sapphire does not interfere with the current conduction in GaN. By selectively removing certain area of GaN, the GaN layer can be separated into multiple electrically isolated small-area LEDs. These LEDs can be connected together by metal interconnects at a later stage, allowing a variety of integrated optoelectronic circuits to be developed.

As GaN is highly resistant to wet etch, dry etch is the conventional technique for the partial or complete removal of GaN. Reactive ion etching (RIE) (Lee, et al. 1995) using CHF_3/Ar and $\text{C}_2\text{ClF}_5/\text{Ar}$ plasmas, for example, can achieve an etch rate between 60 and 470 angstrom/min (Liann-Be, et al. 2001). Inductively coupled plasma (ICP) etching using Cl_2 and Ar, on the other hand, offers an attractive etch rate of up to 1 $\mu\text{m}/\text{min}$ (Smith, et al. 1997). However, dry etch techniques require masking material to cover the regions not to be removed. Typically, with photoresist as an etch mask, the photoresist layer has to be at least as thick as the GaN layer to be etched (Liann-Be, et al. 2001), which is about 3-4 μm . Spin-coating of photoresist layer of this thickness is often cumbersome (for example, edge bead effect may occur (Yang and Chang 2006)), coupled with the fact that thicker photoresists generally offer lower resolutions. Mask thickness can be reduced when hard masks such as SiO_2 are used, but additional lithography and dry etch steps are needed for patterning.

In this section, a maskless direct-write laser micromachining technique for device isolation on GaN-on-sapphire wafer is introduced. Unlike wafer dicing, where GaN and sapphire are to be ablated to complete separation, the laser ablation in our new technique automatically terminates at the GaN/sapphire interface. The principle lies on the large difference between: (1) the ablation thresholds (the minimum laser fluence to achieve ablation), and (2) the optical absorption coefficients at ultraviolet (UV) wavelength of GaN and sapphire, as shown in Table 1.

	GaN	Sapphire
Ablation threshold (J/cm ²)	0.25 (Akane, et al. 1999a; Liu, et al. 2002)	4.5 (Li, et al. 2004)
Optical absorption coefficient (cm ⁻¹)	100000 - 150000 (Muth, et al. 1997)	0.01 - 1 (Patel and Zaidi 1999)

Table 1. Parameters of GaN and sapphire that facilitate selective laser ablation.

When the laser fluence is controlled between the two ablation thresholds, GaN is ablated while sapphire is left undamaged. A simple way to achieve this is by offsetting the wafer from the best focus plane and adjusting the laser spot size. As shown in Figure 12 (a), the laser energy is concentrated to a small spot in the vicinity of the best focus plane. GaN layer (comprising p-type GaN, InGaN/GaN multi-quantum well (MQW) and n-type GaN) and sapphire layer are cut through, which is the mode for die separation. When the focus offset increases, the laser spot is enlarged and the laser fluence is reduced. At a certain range of focus offset, the laser fluence is just high enough to ablate GaN but not sapphire. By scanning the laser across the wafer, a trench terminating at the GaN/sapphire interface is resulted. This is the desired mode for device isolation (Figure 12 (b)). If the focus offset is increased further, the laser fluence will not be sufficient to ablate GaN completely. Device isolation cannot be achieved (Figure 12 (c)).

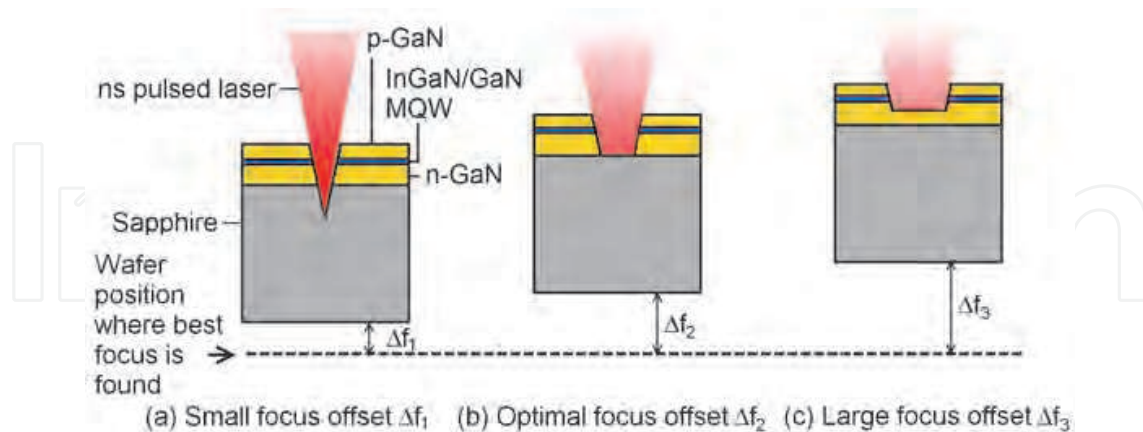


Fig. 12. Control of laser fluence by focus offset. (with permission for reproduction from American Institute of Physics)

A number of factors affect the quality of trenches. In our study, five laser parameters (focus offset, pulse energy, pulse repetition rate, scan speed and number of scan passes) and two ambient media (air and deionized water) were investigated. By the end of this section, two applications of this laser micromachining technique will also be discussed.

3.1 Trench micromachining in air

The laser micromachining experiment was first performed in ambient air at room temperature by using the setup shown in Figure 13 (schematic diagram shown in Figure 2). The laser source was a third-harmonic neodymium-doped yttrium lithium fluoride (Nd:YLF) diode-pumped solid-state (DPSS) laser, with center wavelength of 349 nm and pulse repetition rate of single pulse to 5 kHz. The full-width-at-half-maximum (FWHM) pulse width was 4 ns, while the pulse energy was varied by changing the diode pumping current. The expanded and collimated beam was guided by several laser mirrors and focused onto a piece of GaN-on-sapphire sample (emission wavelength = 470 nm, thickness of GaN = 3 μm and thickness of sapphire = 300 μm) on an XY motorized stage. The fused-silica focusing triplet lens allowed UV and visible light to pass through and had a focal length of 19 mm. As the stage translated while keeping the laser spot stationary, trenches were scribed onto the sample. The scan speed was controlled by software with a precision up to 25 $\mu\text{m}/\text{s}$. The sample could be shifted away from the focus by manually adjusting the stage height. The accuracy of height adjustment was $\pm 5 \mu\text{m}$. A charge-coupled device (CCD) camera was installed confocal to the optical path for real-time observation of the micromachining process. Owing to the high temperature during laser ablation, sedimentary

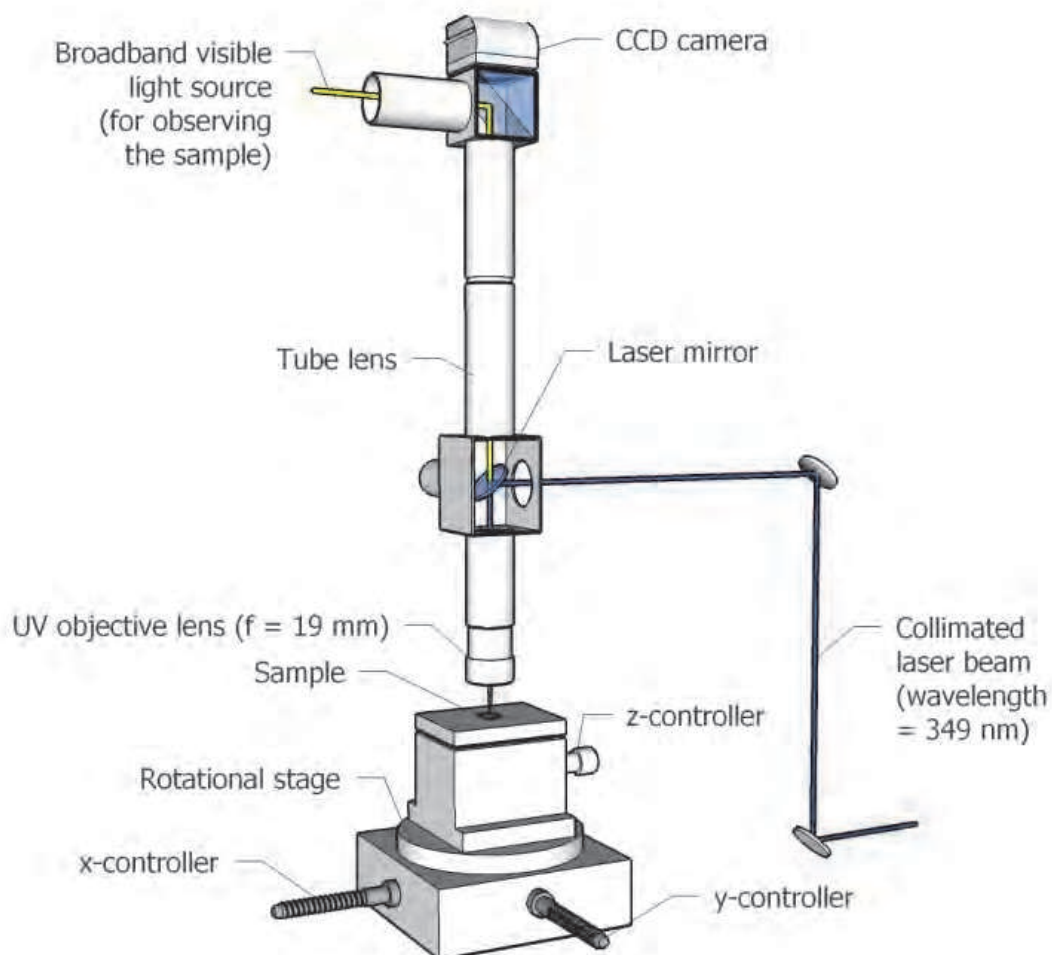


Fig. 13. Experimental setup for laser micromachining in air. (with permission for reproduction from American Institute of Physics)

by-products were formed on the surface of GaN, such as Ga metal (Akane, et al. 1999b; Kelly, et al. 1996) and gallium oxide (Gu, et al. 2006). These substances were effectively removed by sonification of the sample in dilute hydrochloric acid (HCl) (18% by mass) for 15 min. The sample was then rinsed in DI water to remove the remaining acid. The morphology of the resulting trenches were observed by field-emission scanning electron microscopy (FE-SEM), identifying the effect of each laser parameter towards the trench quality.

3.1.1 Focus offset

Figure 14 shows the micromachined trenches at three different focus offset levels while keeping the pulse energy, repetition rate, and scan speed constant. Upward focus offset is taken as positive. The results follow the principle introduced at the beginning of this section. In Figure 14 (a) where the sample is positioned near the best focal plane (300 μm above), the laser beam ablates both the GaN (lighter colour) and sapphire (darker colour). A V-shaped valley is formed in the sapphire layer due to the Gaussian beam shape. Although trenches like these serve the purpose of electrical isolation between adjacent devices, the deep V-shaped valley is not suitable for the conformal deposition of metal interconnect, since the interconnection will become discontinuous at the sharp corners of the valley. At the optimal focal offset plane (450 μm above), as shown in Figure 14 (b), the ablation terminates automatically at the GaN/sapphire interface, exposing a flat and smooth sapphire bottom surface. At a larger focus offset plane of 600 μm , the GaN layer is not completely removed, leaving a shallow and rugged trench on the surface (Figure 14 (c)).

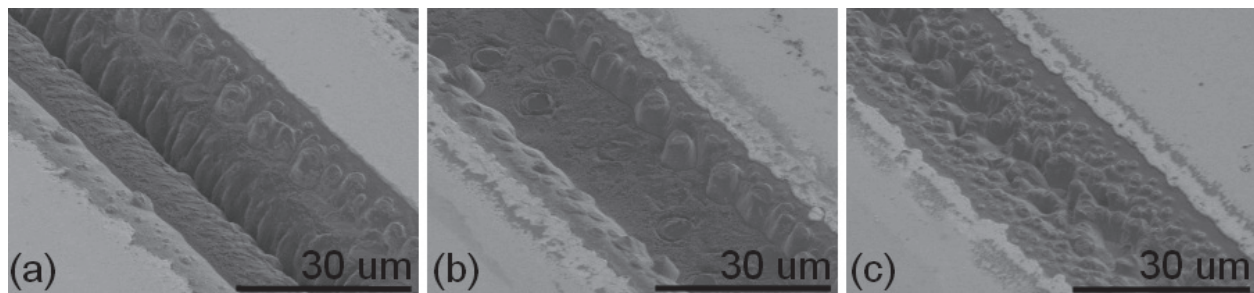


Fig. 14. SEM images of trenches laser micromachined at different focus offset planes: (a) small offset of 300 μm ; (b) optimal offset of 450 μm ; (c) large offset of 600 μm . The pulse energy, pulse repetition rate, and scan speed were fixed at 23 μJ , 1 kHz, and 25 $\mu\text{m/s}$, respectively. (with permission for reproduction from American Institute of Physics)

3.1.2 Pulse energy

Pulse energy is another determining factor of trench quality. Figure 15 illustrates micromachined trenches processed at three different pulse energies between 7 and 45 μJ , while keeping all other parameters constant. The focus offset is kept at the optimal value of 450 μm , as determined from the previous set of experiment. When the pulse energy is set too high, the effect is similar to that of having a smaller focus offset, whereby the GaN as well as sapphire are ablated to form a V-shaped trench (Figure 15 (a)). Similar correspondence between low pulse energy and large focus offset can be observed in Figure 15 (c). Notice that the trench width also increases for higher pulse energy. This property will be further explored in laser micromachining in DI water.

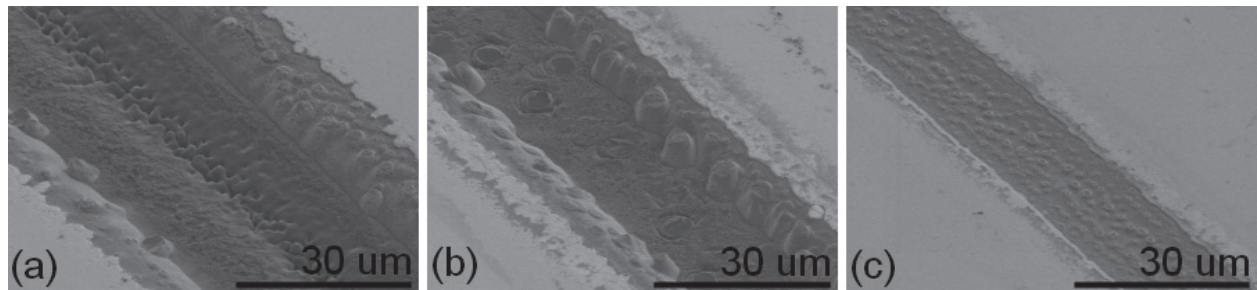


Fig. 15. SEM images of trenches under different pulse energy: (a) higher pulse energy of $45 \mu\text{J}$; (b) optimal pulse energy of $23 \mu\text{J}$; (c) lower pulse energy of $7 \mu\text{J}$. The focus offset level, pulse repetition rate, and scan speed are fixed at $450 \mu\text{m}$, 1 kHz , and $25 \mu\text{m/s}$, respectively. (with permission for reproduction from American Institute of Physics)

3.1.3 Pulse repetition rate

Trenches that are laser-micromachined under an increasing pulse repetition rate are shown in Figure 16 (a)-(c); all other parameters are kept constant. When the pulse repetition rate increases from 1 to 5 kHz , the trench width remains more or less unchanged, but the sidewall and bottom surfaces become increasingly smooth. This observation can be understood in terms of heat accumulation effects and its consequence to the etch efficiency. As the repetition rate increases, cumulative heating by earlier pulses causes localized melting of the material (Schaffer, et al. 2003). This results in an increase in the average surface temperature and thus the removal rate of the ablated materials, minimizing redeposition of debris over the trench.

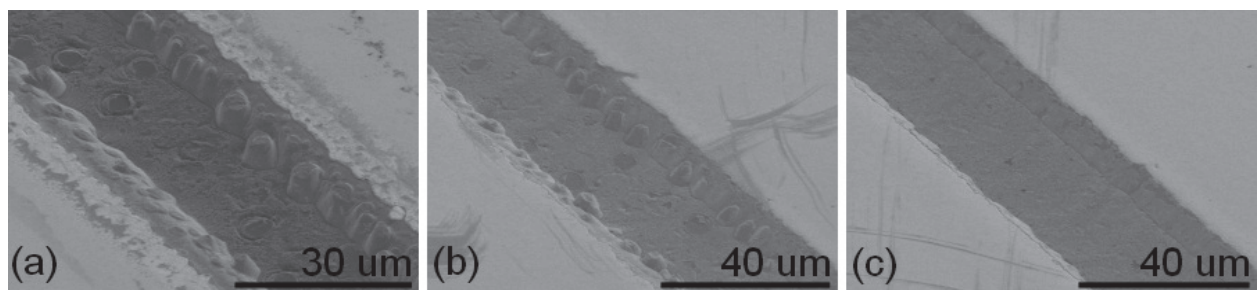


Fig. 16. SEM images of trenches under different pulse repetition rate: (a) 1 kHz ; (b) 3 kHz ; (c) 5 kHz . The focus offset, pulse energy, and scan speed were fixed at $450 \mu\text{m}$, $23 \mu\text{J}$, and $25 \mu\text{m/s}$, respectively. (with permission for reproduction from American Institute of Physics)

3.1.4 Scan speed

The rate at which the laser beam scans across the material is also investigated. From Figure 17, a faster translation rate does not result in a change in the trench width. However, it leads to degradation in the trench quality. At a faster translation speed, the exposure time to the laser light at each position becomes shorter. There is not enough time for temperature rise and/or photon-matter interaction. Stalagmite-like structures begin to appear around the sidewalls.

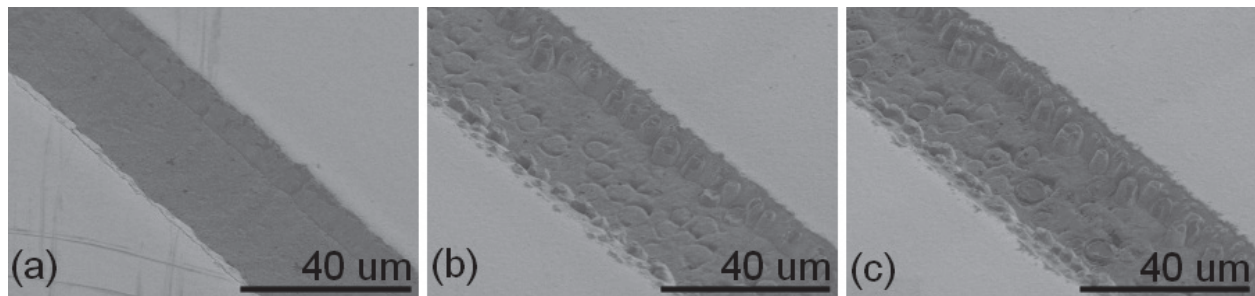


Fig. 17. SEM images of trenches under different scan speeds: (a) 25 $\mu\text{m/s}$; (b) 75 $\mu\text{m/s}$; (c) 125 $\mu\text{m/s}$. The focus offset, pulse energy, and repetition rate were kept at 450 μm , 23 μJ , and 5 kHz, respectively. (with permission for reproduction from American Institute of Physics)

3.1.5 Number of scan passes

The remaining factor to consider is the number of scans. Similar to the effect of increasing scan speed, an increase in the number of scans does not alter the trench width. However, a narrow groove is formed at the center of the trenches for three and five passes, as illustrated in Figure 18 (b) and (c), respectively. There is also no remarkable improvement in the sidewall and bottom surface quality.

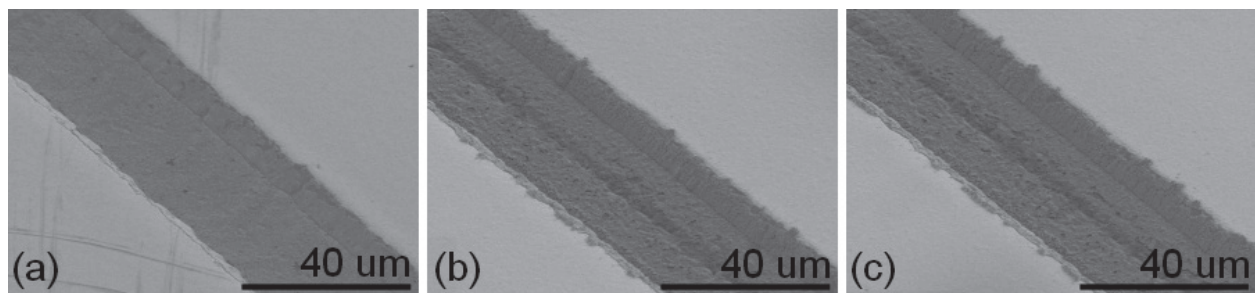


Fig. 18. SEM images of trenches under different number of scan passes: (a) single pass; (b) three passes; (c) five passes. The focus offset, pulse energy, repetition rate and scan speed were kept at 450 μm , 23 μJ , 5 kHz, and 25 $\mu\text{m/s}$, respectively. (with permission for reproduction from American Institute of Physics)

Through the above experiments, we can conclude that an optimal combination of focus offset and pulse energy, higher pulse repetition rate, slower scan speed and single pass of scan are essential for good trench quality. Nevertheless, substantial amount of redeposition and resolidification of ablated material still exists on the trench bottom surface and sidewall when the process is performed in air. This is the result of thermal ablation and photochemical ablation mechanisms of nanosecond lasers. Although the redeposition can be effectively removed by strong acids, this is not feasible when the underlying material also reacts with the acids. In order to reduce the heat load during ablation, laser micromachining with the sample immersed in a liquid is proposed. Criteria for the liquid include good thermal conductivity and high specific heat capacity. In addition, the attenuation of UV and visible light in that liquid should be low, so that laser energy can be transferred efficiently to the substrate and the micromachining process can be monitored concurrently. DI water would be a good choice to match these criteria. The mechanisms involved in the liquid-immersion laser micromachining of GaN will be investigated in the following subsection.

3.2 Trench micromachining in DI water

The characteristics of liquid-immersion laser micromachining for GaN were investigated experimentally using the optical setup shown in Figure 19. The setup was similar to that used for ambient air (Figure 13), except that the GaN-on-sapphire sample was immersed horizontally in a DI water bath with meniscus about 1 mm above the sample surface. Although thicker water layer can improve heat dissipation, attenuation of the laser beam will become more severe. On the other hand, the water layer cannot be too thin since the entire sample will not be wetted under the strong surface tension of water. The water bath was placed on the manual Z translation stage, mounted on the motorized XY translation stage to enable laser scanning. The laser fluence was again adjusted by offsetting the sample surface from the best focal plane. Besides observing the surface morphology by FE-SEM, the trench surface roughness was measured by atomic force microscopy (AFM). Elemental analysis of the trench surface was performed by the energy-dispersive X-ray spectroscopy (EDX) function offered by the FE-SEM.

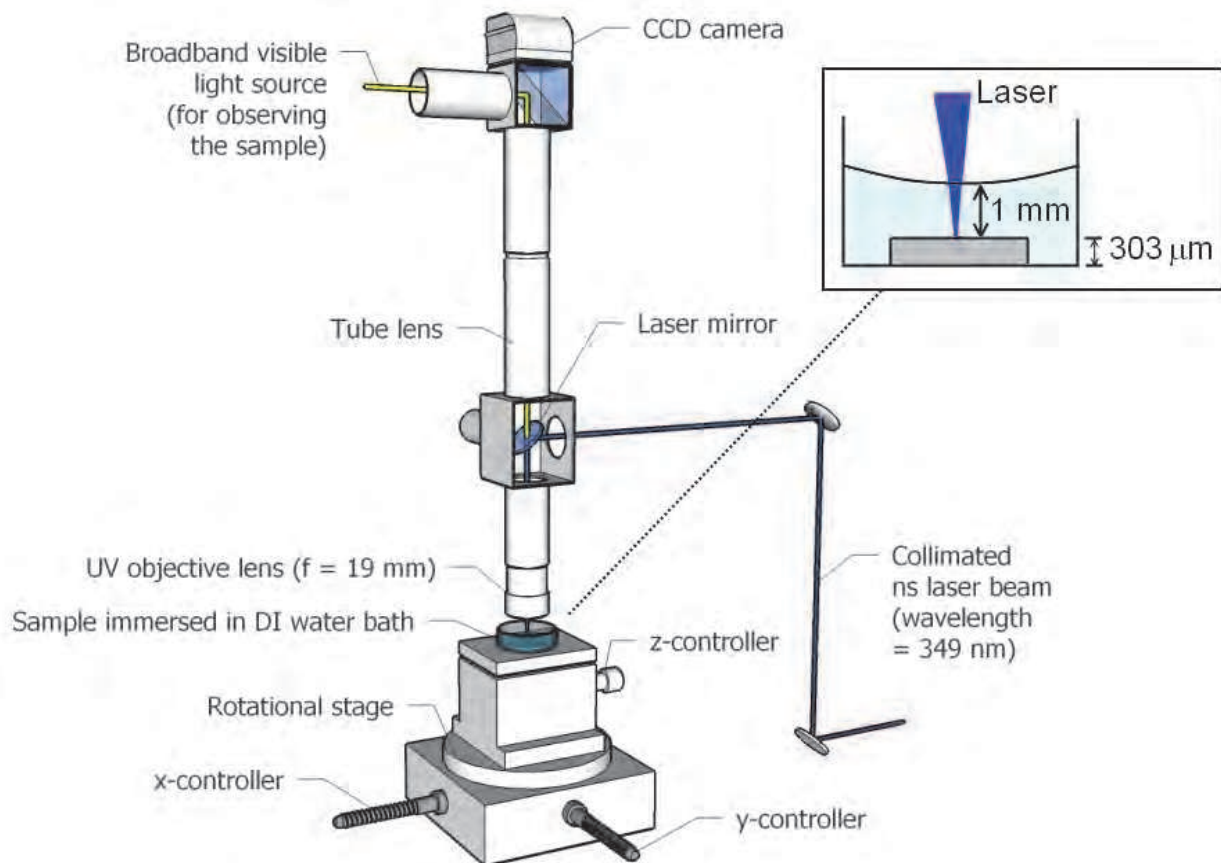


Fig. 19. Experimental setup for laser micromachining in DI water. (with permission for reproduction from Springer)

3.2.1 Trench quality as compared with ambient air

Compared with laser micromachining in ambient air, DI water is capable of producing trenches with substantially smoother sidewalls and bottom surfaces. Figure 20 shows AFM scans of the trenches generated in both ambient media. By measuring the height values y_i

along the trench edge, the sidewall roughness R_a is determined by taking the arithmetic average of the absolute height deviation from the mean height. The trench micromachined in air has an R_a of 312 nm, contrasting sharply with 27.65 nm for the trench produced in DI water. The rms roughness of the bottom surfaces also reveals the superiority of liquid immersion (87.49 nm for air vs. 13.42 nm for DI water). As a comparison with inorganic material whose laser-matter interaction should be similar to that of GaN, we quoted that the R_a value of microchannels micromachined by femtosecond laser in aluminosilicate glass sheet in ambient air is approximately 40 nm (Zheng, et al. 2-006). This indicates that nanosecond laser micromachining in DI water can have comparable performance with femtosecond laser micromachining in air.

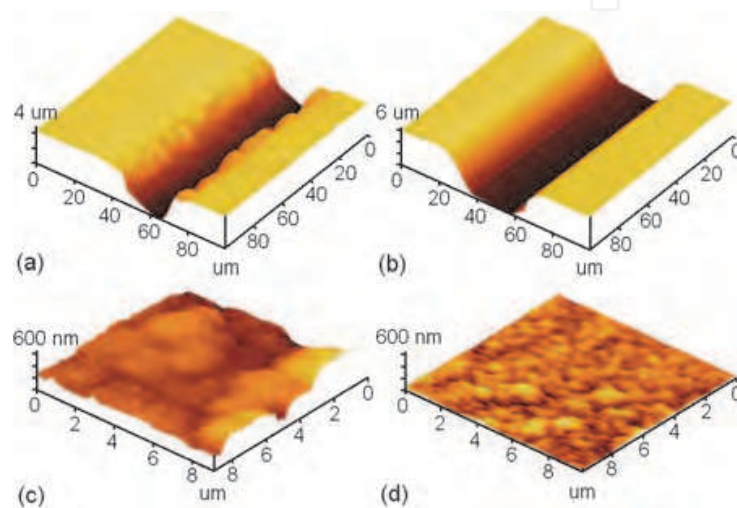


Fig. 20. AFM scans of trenches generated in: (a) and (c) air; (b) and (d) DI water. (c) and (d) are the zoomed-in images of the bottom surfaces. The focus offset, pulse energy, pulse repetition rate, scan speed were fixed at 400 μm , 25 μJ , 1 kHz and 25 $\mu\text{m}/\text{s}$. Only single pass of scan was performed. (with permission for reproduction from Springer)

Liquid-immersion laser micromachining also results in trenches of quality comparable to conventional lithographic and ICP deep etch processes. From the SEM images of sidewalls around ICP-etched regions in the literature (Ladroue, et al. 2010; Qiu, et al. 2011), we see that the smoothness is comparable to that of the laser-micromachined trench sidewalls. Besides, striations are observed over the sidewalls of ICP-etched regions when Ni hard mask is used. This is not observed in liquid-immersion laser micromachining, as shown in Figure 20 (b). Though SiO_2 hard mask can be used to eliminate the striations in ICP, it comes with the price of sidewall steepness reduction.

As a demonstration of reduced redeposition, the EDX results of the trench bottom surface are shown in Table 2. Three elements were found: O, Al and Ga. Al and O are the constituent elements of sapphire (Al_2O_3), whereas Ga is a product from the thermal decomposition of GaN during laser ablation (Ambacher, et al. 1996; Choi, et al. 2002). It is found that there is a lower percentage of Ga over those trenches produced in DI water. It should be noted that while the sample for air had been sonicated in dilute HCl before EDX examination, that for DI water was not subjected the same treatment. The results indicate that liquid immersion is effective in ejecting the molten Ga (m.p. = 29.76°C, b.p. = 2204°C) from the irradiated site and preventing its resolidification around the trench.

	Air	DI water
O	64.67%	65.19%
Al	34.81%	34.65%
Ga	0.52%	0.16%

Table 2. Atomic composition of trench bottom surface.

Besides improved surface quality, liquid-immersion laser micromachining also offers two advantages with respect to process control. The first is increased focus offset tolerance. Figure 21 (a)-(c) show three trenches micromachined in ambient air. When the sample position deviates from the optimum plane (Figure 21 (b)) by 150 μm , either damage to the sapphire layer (Figure 21 (a)) or incomplete trench (Figure 21 (c)) occurs. For micromachining in DI water, the trench quality is not compromised even with a deviation as large as 200 μm , albeit a slight decrease in the trench width (Figure 21 (d)-(f)). The second advantage of liquid immersion is the control over trench width by varying pulse energy. Owing to the focus offset tolerance, the variation of pulse energy does not significantly compromise the trench quality. Figure 22 shows an approximately linear relationship between pulse energy and trench width when performing micromachining in DI water at a fixed focus offset. For micromachining in ambient air, it is difficult to control the trench width just by altering the pulse energy. This is because the optimum focus offset depends strongly on the pulse energy. A new optimum focus offset needs to be found when the pulse energy is altered.

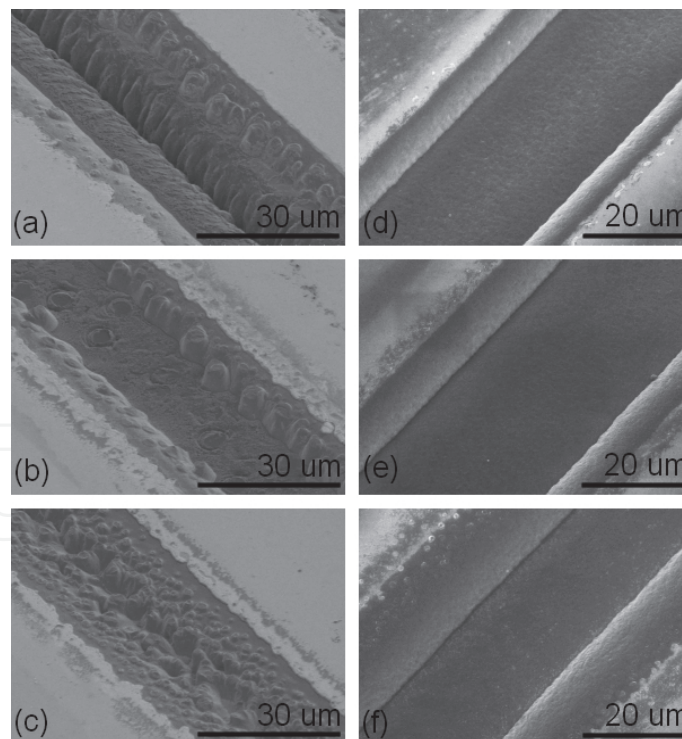


Fig. 21. SEM images of trenches laser-micromachined at different focus offset planes: (a)-(c) in air: (a) 300 μm , (b) 450 μm , (c) 600 μm , where 450 μm is the optimum; (d)-(f): in DI water: (d) 300 μm ; (e) 500 μm ; (f) 700 μm , where 500 μm is the optimum. The pulse energy, pulse repetition rate and scan speed were fixed at 25 μJ , 1 kHz and 25 $\mu\text{m/s}$. (with permission for reproduction from Springer)

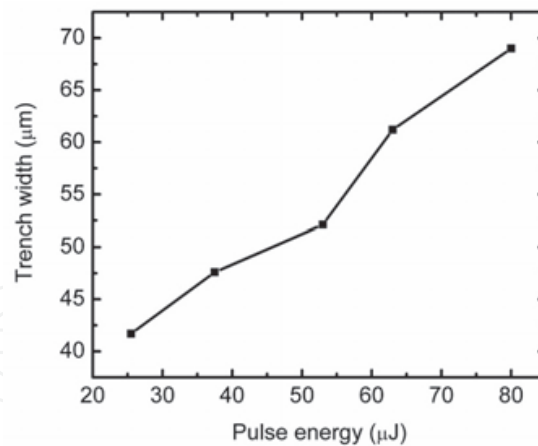


Fig. 22. Trench width control by varying pulse energy. The focus offset, pulse repetition rate and scan speed were fixed at 550 μm, 1 kHz and 25 μm/s. (with permission for reproduction from Springer)

3.3 Theoretical discussions

The improved trench quality can be explained in terms of the following processes during the nanosecond-pulsed laser ablation of GaN: Heat transfer, plasma-induced recoil pressure, plasma shielding effect in water and collapse of cavitation bubbles.

3.3.1 Heat transfer

Referring to Table 3, DI water has a much higher specific heat capacity and thermal conductivity than air. Therefore DI water is expected to carry the excess heat away from the irradiated region faster than air. To verify this, a simulation on the heat conduction process for single-pulse irradiation was performed. The heat equation (in cylindrical coordinates) was solved by finite element method (FEM):

$$\rho c \frac{\partial T}{\partial t} - \nabla \cdot (k \nabla T) = Q \quad (2)$$

where ρ , c and k are as defined in Table 3, T is the temperature distribution (K) and Q represents the heat source ($W \text{ mm}^{-3}$). Q originates from the Gaussian laser beam, thus both Q and the resulting T are assumed to be radially symmetric. The domain and boundary conditions are defined in Figure 23. Without going into the details, the simulation results are presented as follows. Figure 24 shows the variation of GaN surface temperature during the initial 100 ns at the center of the laser spot ($r = 0, z = 0$) (solid curves) and near the trench edge ($r = 15 \mu\text{m}, z = 0$) (dotted curves). The GaN surface temperature in air is found to be higher than that in DI water at both positions. In addition, sharper temperature peaks are found when the micromachining is performed in air. The maximum temperature is as high as 1000°C even near the trench edge. It is known that GaN begins to decompose into liquid Ga and N_2 gas at a temperature of 900°C (Choi, et al. 2002). The rapid heating and cooling cycles in air can result in the increased generation and resolidification of molten Ga within each pulse period. The resolidified Ga droplets deposit around the sidewall, degrading the surface quality. Another consequence of rapid heating and cooling is the increased thermal stress incurred in the crystal structure of GaN. Cracks may be resulted.

	ρ (g cm ⁻³)	c (J g ⁻¹ °C ⁻¹)	k (W cm ⁻¹ °C ⁻¹)
GaN	6.15	0.49	1.3
Al ₂ O ₃	4.025	0.75	0.35
H ₂ O	1.0	4.18 (at 25°C)	0.006
Air	1.184 × 10 ⁻³	1.012 (at 23°C)	2.5 × 10 ⁻⁴

Table 3. Density ρ , specific heat capacity c and thermal conductivity k of the substances involved in the laser micromachining process.

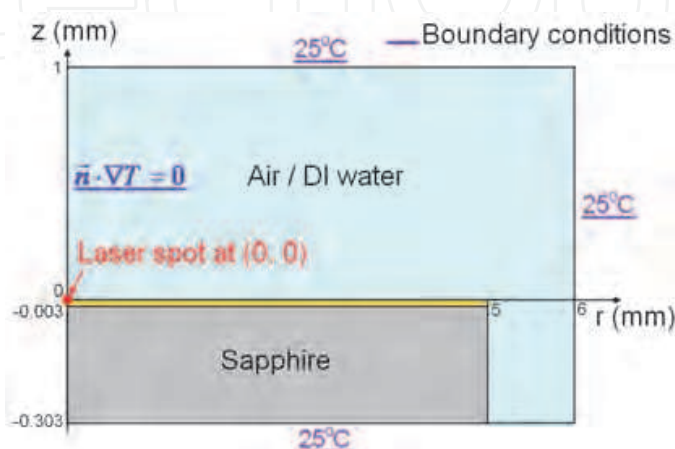


Fig. 23. Simulation domain. (with permission for reproduction from Springer)

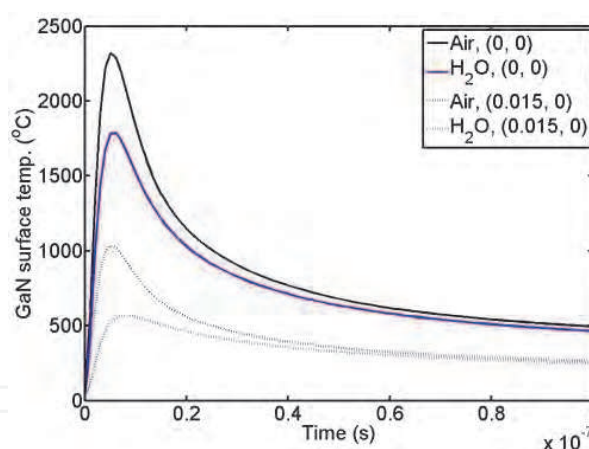


Fig. 24. Temporal variation of GaN surface temperature at two different positions: at the center of laser spot (solid); near the edge of the trench (dotted). (with permission for reproduction from Springer)

The two-dimensional temperature distribution also demonstrates the strong cooling effect of water. As shown in Figure 25, at $t = 1 \mu\text{s}$, the temperature of water immediately above the sample surface is lower than that of air. The slight decrease of water temperature below the room temperature can be attributed to the adiabatic expansion of water vapour as well as the vapour plume of ablated material (Gusarov, et al. 2000). At this instance, the GaN surface temperature in water is in general lower than that in air, indicating efficient heat extraction by water. The heat-affected zone (HAZ) is also seen to be smaller when the sample is immersed in DI water.

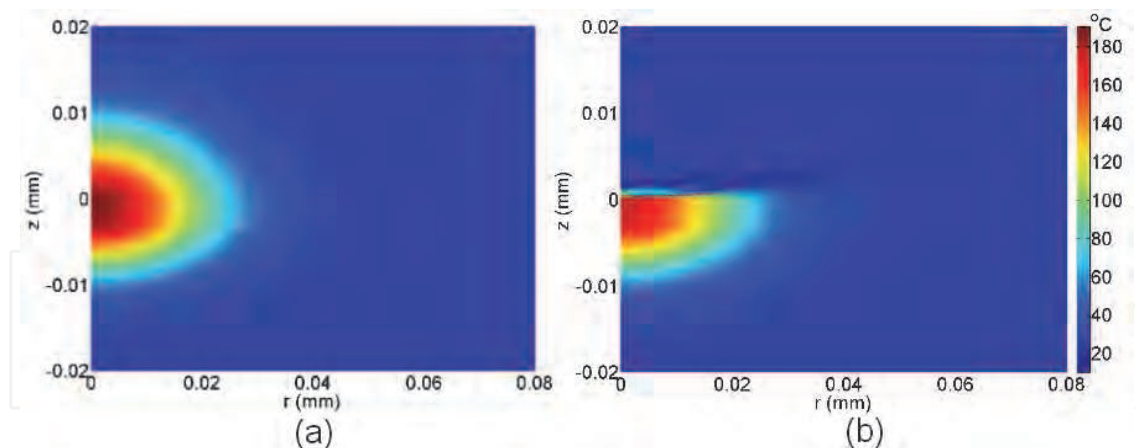


Fig. 25. Temperature distribution at $t = 1 \mu\text{s}$ when the ambient medium is: (a) air; (b) DI water. (with permission for reproduction from Springer)

3.3.2 Plasma-induced recoil pressure

High-energy laser pulses are able to melt, vaporize and ionize the material being irradiated, resulting in the formation of plasma. When the plasma expands, a recoil pressure is exerted on the sample surface, causing material removal. If the ambient medium is water instead of air, the expansion of plasma will be confined by the underwater pressure. This leads to an increase in the plasma-induced recoil pressure and higher removal rate of material.

3.3.3 Plasma shielding effect in water

The plasma generated from laser ablation can absorb part of the incident laser energy and reduce the energy delivered to the sample. This is known as plasma shielding effect. The effect becomes stronger when the plasma has a larger size, longer duration and a starting time that overlaps with the laser pulse. Because of water confinement effects, the plasma size and duration are much reduced in water. The onset of plasma formation is also delayed by 5 ns, reducing the overlap time between the laser pulse and the plasma (Hong, et al. 2002). These factors weaken the plasma shielding effect, causing a stronger coupling of the laser beam with the material. Material removal is thus more efficient in water.

3.3.4 Collapse of cavitation bubbles

Formation of cavitation bubbles is a process that happens solely in liquids. In the experiment, the bubbles may originate from the dissolved gases in DI water, or the N_2 gas from the laser ablation of GaN. When a bubble collapses near the sample surface, a high-speed liquid jet directed towards the surface will be generated. If there is no water between the bubble and sample surface, the liquid jet will produce a strong impulse towards the sample. This impulse can be 5.2-12.4 times that of the laser ablation impact in air (Lu, et al. 2004), which further helps the liquid-phase expulsion of Ga.

3.4 Applications

To close this section, two applications of liquid-immersion laser micromachining are introduced: alternating-current LED (ac-LED) and 5×7 dot-matrix microdisplay. Ac-LED is an LED chip that is directly powered by an ac voltage. The basic idea is to make use of the diode property of LEDs to construct an on-chip bridge rectifier. The rectified voltage is then

used to power other on-chip LEDs. The plan view of the chip overlaid with the circuit diagram is shown in Figure 27 (a). The on-chip LEDs are isolated by the trenches from liquid-immersion laser micromachining. This chip is designed to work on 12 V_{rms} , but the design can be easily extended to higher voltages. Its full operation is shown in Figure 26 (b). The other application, dot-matrix microdisplay, also requires laser micromachining to separate rows of LED pixels (Figure 27 (a) and (b)). Narrow trenches are formed by low pulse energy, allowing pixels to be packed more closely together. By controlling the on-off sequence of pixels, alphanumeric characters can be formed, as shown in Figure 27 (c).

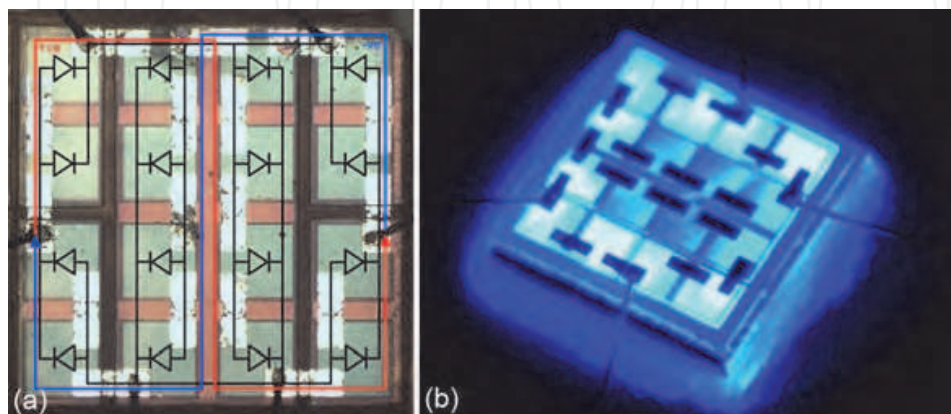


Fig. 26. Microphotograph of ac-LED, with circuit diagram superimposed. The directions of current flow during the positive and negative cycles of ac voltage are shown with red and blue arrows respectively; (b) Microphotograph of ac-LED operating under an ac voltage of 12 V_{rms} . (with permission for reproduction from American Institute of Physics)

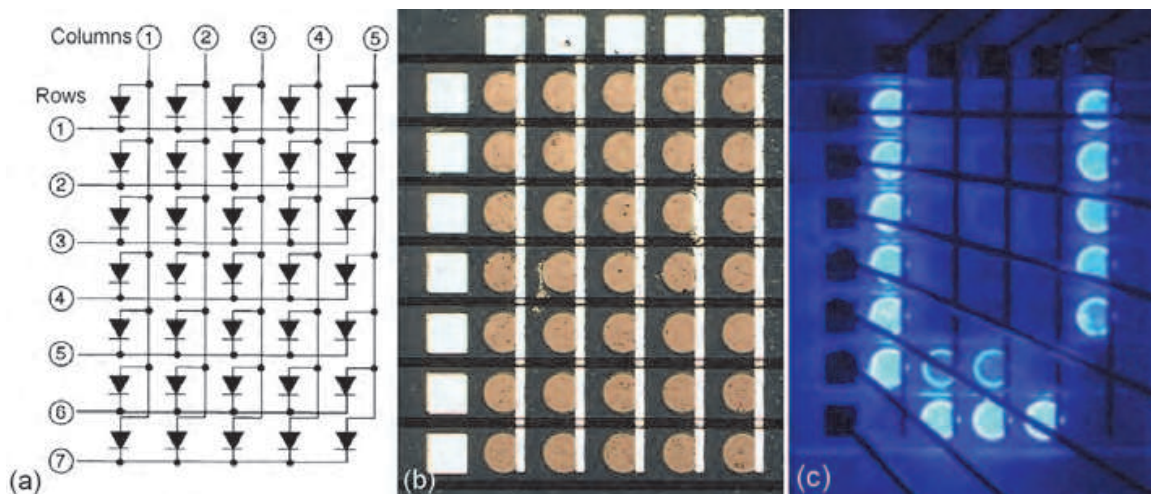


Fig. 27. Circuit diagram of 5×7 dot-matrix microdisplay; (b) Microphotograph of the microdisplay chip; (c) Microdisplay in operation, showing the character "U".

4. Conclusion

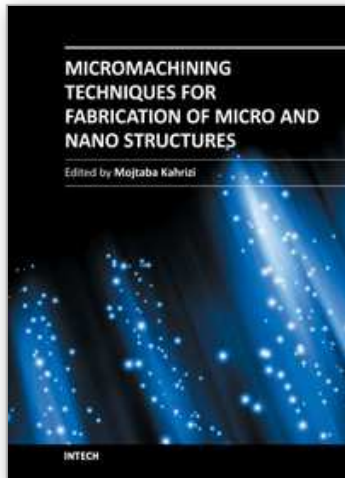
Laser micromachining involving a nanosecond diode-pumped solid-state laser at 349 nm wavelength is developed for device fabrication of light-emitting diodes on sapphire wafer. The material ablation process can be readily controlled and optimized for varied

micromachining purposes such as wafer cutting featuring high aspect ratios and precision etching for device isolation. Highest aspect ratio of the cleave on GaN/sapphire wafer is achieved by front side laser micromachining method with the beam focused at the GaN layer. With laser micromachining process optimized for chip shaping, novel chip geometry such as truncated pyramid and triangular LED is fabricated and the novel LED geometries effectively improve light extraction efficiency. Influence of ambient medium as well as effects of various process parameters are taken into account to develop a reliable laser micro-patterning process. The laser beam, focused with a shorter focal length focusing lens, is tuned to selectively etch conductive GaN layers on the insulating sapphire substrate generating isolation grooves with desired profile and pattern that facilitates further processing.

5. References

- Akane, T., K. Sugioka, and K. Midorikawa 1999a High-speed etching of hexagonal GaN by laser ablation and successive chemical treatment. *Applied Physics A (Materials Science Processing)* A69.
- Akane, T., et al. 1999b KrF excimer laser induced ablation-planarization of GaN surface. *Applied Surface Science* 148(1-2).
- Ambacher, O., et al. 1996 Thermal stability and desorption of group III nitrides prepared by metal organic chemical vapor deposition. *Journal of Vacuum Science & Technology B (Microelectronics and Nanometer Structures)* 14(6).
- Choi, H. W., et al. 2002 Surface analysis of GaN decomposition. *Semiconductor Science and Technology* 17(12).
- Fu, W. Y., et al. 2009 Geometrical Shaping of InGaN Light-Emitting Diodes by Laser Micromachining. *Ieee Photonics Technology Letters* 21(15):1078-1080.
- Gattass, Rafael R., and Eric Mazur 2008 Femtosecond laser micromachining in transparent materials. *Nature Photonics* 2(4):219-225.
- Gu, E., et al. 2006 Microfabrication in free-standing gallium nitride using UV laser micromachining. *Applied Surface Science* 252(13):4897-4901.
- Gusarov, A. V., A. G. Gnedovets, and I. Smurov 2000 Two-dimensional gas-dynamic model of laser ablation in an ambient gas. *Applied Surface Science* 154-155.
- Hong, M. H., et al. 2002 Steam-assisted laser ablation and its signal diagnostics. *Applied Surface Science* 197-198.
- Kelly, M. K., et al. 1996 Optical patterning of GaN films. *Applied Physics Letters* 69(12).
- Ladroue, J., et al. 2010 Deep GaN etching by inductively coupled plasma and induced surface defects. *Journal of Vacuum Science & Technology A: Vacuum, Surfaces, and Films* 28:1226.
- Lee, H., D.B. Oberman, and J.S. Harris Jr 1995 Reactive ion etching of GaN using CHF₃/Ar and C₂F₄/Ar plasmas. *Appl. Phys. Lett* 67:1754.
- Li, X. X., et al. 2004 Ablation induced by femtosecond laser in sapphire. *Applied Surface Science* 225(1-4):339-346.
- Liann-Be, Chang, Liu Su-Sir, and Jeng Ming-Jer 2001 Etching selectivity and surface profile of GaN in the Ni, SiO₂ and photoresist masks using an inductively coupled plasma. *Japanese Journal of Applied Physics, Part 1 (Regular Papers, Short Notes & Review Papers)* 40(3A).

- Liu, Wei-Min, et al. 2002 Ablation of GaN using a femtosecond laser. *Chinese Physics Letters* 19(11).
- Liu, X., D. Du, and G. Mourou 1997 Laser ablation and micromachining with ultrashort laser pulses. *Ieee Journal of Quantum Electronics* 33(10):1706-1716.
- Lu, J., et al. 2004 Mechanisms of laser drilling of metal plates underwater. *Journal of Applied Physics* 95(8):3890-3894.
- Molian, P., B. Pecholt, and S. Gupta 2009 Picosecond pulsed laser ablation and micromachining of 4H-SiC wafers. *Applied Surface Science* 255(8):4515-4520.
- Muth, JF, et al. 1997 Absorption coefficient, energy gap, exciton binding energy, and recombination lifetime of GaN obtained from transmission measurements. *Applied Physics Letters* 71:2572.
- Patel, BS, and ZH Zaidi 1999 The suitability of sapphire for laser windows. *Measurement Science and Technology* 10:146.
- Qiu, Rongfu, et al. 2011 Optimization of inductively coupled plasma deep etching of GaN and etching damage analysis. *Applied Surface Science* 257(7).
- Schaffer, C. B., et al. 2001 Micromachining bulk glass by use of femtosecond laser pulses with nanojoule energy. *Optics Letters* 26(2):93-5.
- Schaffer, C. B., J. F. Garcia, and E. Mazur 2003 Bulk heating of transparent materials using a high-repetition-rate femtosecond laser. *Applied Physics a-Materials Science & Processing* 76(3):351-354.
- Smith, SA, et al. 1997 High rate and selective etching of GaN, AlGa_N, and AlN using an inductively coupled plasma. *Applied Physics Letters* 71(25):3631-3633.
- Stuart, B. C., et al. 1996 Nanosecond-to-femtosecond laser-induced breakdown in dielectrics. *Physical Review B* 53(4):1749-1761.
- Varel, H., et al. 1997 Micromachining of quartz with ultrashort laser pulses. *Applied Physics A (Materials Science Processing)* 65(4-5).
- Yang, Y.K., and T.C. Chang 2006 Experimental analysis and optimization of a photo resist coating process for photolithography in wafer fabrication. *Microelectronics Journal* 37(8):746-751.
- Zheng, H. Y., et al. 2006 Ultrashort pulse laser micromachined microchannels and their application in an optical switch. *International Journal of Advanced Manufacturing Technology* 27(9-10):925-929.
- Zweig, A. D. 1991 A thermomechanical model for laser ablation. *Journal of Applied Physics* 70(3):1684-1691.



Micromachining Techniques for Fabrication of Micro and Nano Structures

Edited by Dr. Mojtaba Kahrizi

ISBN 978-953-307-906-6

Hard cover, 300 pages

Publisher InTech

Published online 03, February, 2012

Published in print edition February, 2012

Micromachining is used to fabricate three-dimensional microstructures and it is the foundation of a technology called Micro-Electro-Mechanical-Systems (MEMS). Bulk micromachining and surface micromachining are two major categories (among others) in this field. This book presents advances in micromachining technology. For this, we have gathered review articles related to various techniques and methods of micro/nano fabrications, like focused ion beams, laser ablation, and several other specialized techniques, from esteemed researchers and scientists around the world. Each chapter gives a complete description of a specific micromachining method, design, associate analytical works, experimental set-up, and the final fabricated devices, followed by many references related to this field of research available in other literature. Due to the multidisciplinary nature of this technology, the collection of articles presented here can be used by scientists and researchers in the disciplines of engineering, materials sciences, physics, and chemistry.

How to reference

In order to correctly reference this scholarly work, feel free to copy and paste the following:

Xianghua Wang, Giuseppe Yickhong Mak and Hoi Wai Choi (2012). Laser Micromachining and Micro-Patterning with a Nanosecond UV Laser, *Micromachining Techniques for Fabrication of Micro and Nano Structures*, Dr. Mojtaba Kahrizi (Ed.), ISBN: 978-953-307-906-6, InTech, Available from: <http://www.intechopen.com/books/micromachining-techniques-for-fabrication-of-micro-and-nano-structures/laser-micromachining-and-micro-patterning-with-a-nanosecond-uv-laser>

INTECH
open science | open minds

InTech Europe

University Campus STeP Ri
Slavka Krautzeka 83/A
51000 Rijeka, Croatia
Phone: +385 (51) 770 447
Fax: +385 (51) 686 166
www.intechopen.com

InTech China

Unit 405, Office Block, Hotel Equatorial Shanghai
No.65, Yan An Road (West), Shanghai, 200040, China
中国上海市延安西路65号上海国际贵都大饭店办公楼405单元
Phone: +86-21-62489820
Fax: +86-21-62489821

© 2012 The Author(s). Licensee IntechOpen. This is an open access article distributed under the terms of the [Creative Commons Attribution 3.0 License](#), which permits unrestricted use, distribution, and reproduction in any medium, provided the original work is properly cited.

IntechOpen

IntechOpen